UNIVERSITY of CALIFORNIA
SANTA CRUZ

REAL-TIME DATA COLLECTION AND DISSEMINATION FROM THE BALLOON ARRAY FOR RBSP RELATIVISTIC ELECTRON LOSSES

A thesis submitted in partial satisfaction of the
requirements for the degree of

BACHELOR OF SCIENCE

in

PHYSICS

by

Warren Z. Rexroad

June 2011

The thesis of Warren Z. Rexroad is approved by:

Professor David Smith
Advisor

Professor Adriane Steinacker
Theses Coordinator

Professor David P. Belanger
Chair, Department of Physics

Abstract

Real-Time Data Collection and Dissemination from

The Balloon Array for RBSP Relativistic Electron Losses

by

Warren Z. Rexroad

The Balloon Array for RBSP Relativistic Electron Losses (BARREL) will be flying two Antarctic balloon campaigns during the Austral summer seasons of 2012 and 2013. The objective of these flights will be to investigate the primary mechanisms for relativistic electron losses from the outer radiation belt. It is believed that electromagnetic ion cyclotron waves generated in the plasmasphere are responsible for the long timescale events seen on the duskside. Relativistic microbursts have been recorded in satellite data as very short timescale events thought to be caused by large-amplitude whistler-mode waves. An overview of these wave-particle interactions is presented herein along with a strategy that has been implemented to collect and disseminate BARREL balloon data in real time. Finally a brief summary resulting from our recent test flights is given.

Contents

List of Figures

Acknowledgements

Thank you to David Smith for contributing my scientific knowledge in this field and bringing me onto this project; Max Commes and Andrew Liang for helping me produce the best quality product I could; Michael McCarthy for providing working code for me to build on and ask many, many questions about; and to the rest of the BARREL team for giving me such a great opportunity.

1 Introduction

In 1958 the United States entered the Space Age by launching the first Earth orbiting craft with the Explorer Missions. For several months, Explorer 1 circled the Earth collecting many types of data but one of the most interesting results of this flight came from the on board Geiger counter. At certain altitudes and locations around the Earth it would return an expected 30counts/second from cosmic rays. Interestingly, at other locations this reading would drop to zero. This strange result was confirmed in later Explorer missions and eventually determined to be caused the radiation becoming so great that the Geiger counter became saturated and stopped working. What these mission had discovered became known as the Van Allen Radiation Belt. [Van Allen, 1959]

At the center of the Earth there is a molten core of circulating ions. This motion creates an electric current flowing through the core which generates the Earth's magnetic field known as the magnetosphere. This is approximated to first order as a dipole magnet shown in Figure 1.1. Charged particles traveling through space can become trapped along the field lines creating torus of energetic electrons and protons forming the radiation belt. As it turns out there are actually two belts, a stable inner belt consisting of lower energy protons, and a dynamic outer belt consisting primarily of high energy (relativistic) electrons. [Schindler, 2007]

When charged particles encounter a magnetic field, any component of their velocity that is perpendicular to the field will cause the particle to move in a helix towards the pole. This is called cyclotron motion and is governed by the strength of the magnetic field and the pitch angle of the incoming particle. As the charged particle follows the field line to the pole, the lines converge which

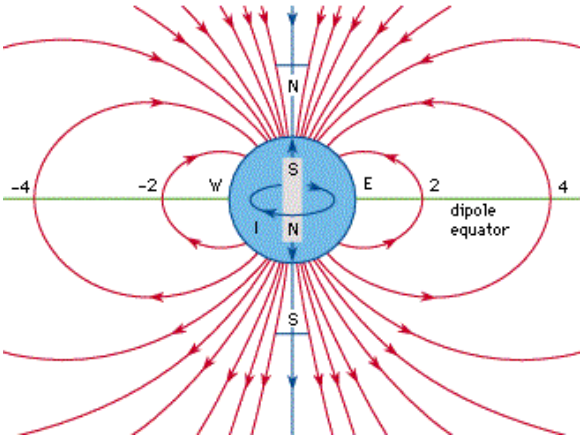

Figure 1.1: First-order approximation of Magnetosphere as a dipole. Taken from Encyclopedia Britanica Online.

increases the strength of the magnetic field. This increased field strength will cause the cyclotron motion of the particle to be increased as well. If the pitch angle is large enough, this motion can actually become so great that the particle is reflected back away from the pole and back into space. [Schindler, 2007] The processes governing trapped particle motion are described in Section 2.5.

This dipole model of the magnetosphere, however, is over simplified. As in Figure 1.2, the Sun blows the magnetosphere away creating a compressed field facing the Sun (the dawn side) and an elongated tail. This tail section is very dynamic and is one major source of disturbances. As the solar wind blows the tail, it gets increasingly longer until it is pinched off and a plasmoid is released. Section 2.2 describes that this processes causes the magnetosphere to reorganize itself so it looks much like the dipole model in Figure 1.1. This dipolarization is accompanied by large releases of energy that can accelerate the contained particles to relativistic energy levels. [Schindler, 2007, Goldstein, 2006, Miyashita et al., 2009]

Even though in a static situation electrons will be trapped in the outer belt, because of dynamics between the Earth and Sun both the energy and population levels are very unstable. There are a number of mechanisms which are reviewed in Section 2.4 that can cause losses from the belt to our atmosphere. In addition to losses, the solar activity as described in Sections 2.1 and 2.2 can create large disturbances in the magnetosphere, accelerating the trapped particles to relativistic

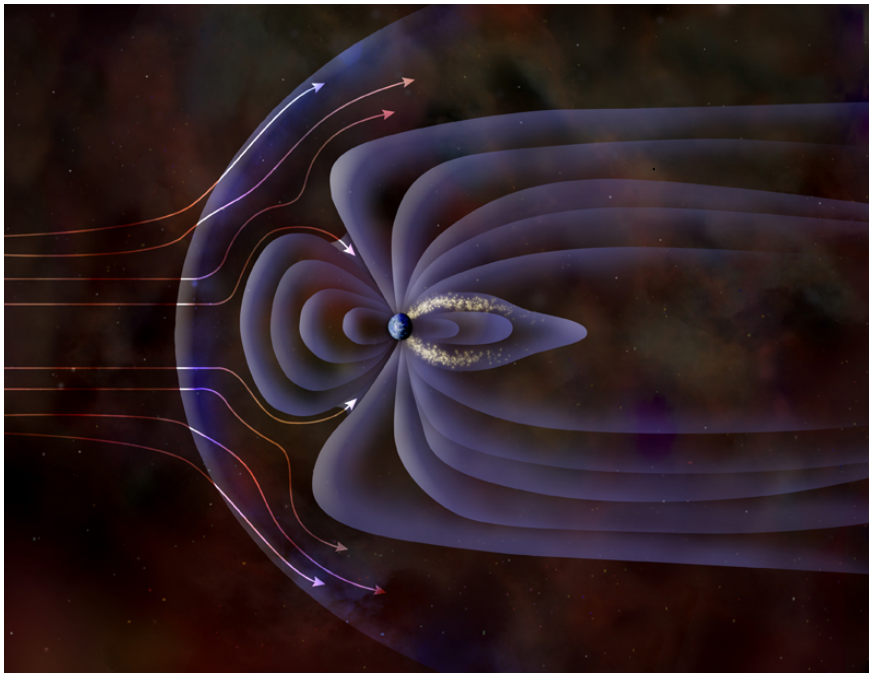

Figure 1.2: Magnetosphere distortion by solar wind. Illustration: NASA/CXC/M.Weiss

energies. The resulting high energy particles are very dangerous to astronauts and can easily damage the sensitive equipment involved in space exploration [Walters et al., 2011]. Figure 1.3 shows how a solar cell designed for satellite use can be degraded by energetic particles.

The ability to predict these disturbances and electron precipitation have thus become a matter of urgency. In an effort to increase our understanding of these dynamics, NASA will be launching the Radiation Belt Storm Probe (RBSP) which will study such events. One of the mission's goals will be to measure precipitation of relativistic electrons into our atmosphere. [Ukhorskiy et al., 2010] A single space probe, however, will not be sufficient to determine how many electrons actually enter the atmosphere.

Determining if the electrons are lost to the atmosphere requires a measurement of its pitch angle relative to the nearby field line. At the altitude of RBSP, this angle must be less than 7° for the electron to be lost. To be able to detect such a small pitch would require a much higher resolution measurement than can be made in situ, leading to the need for a second probe closer

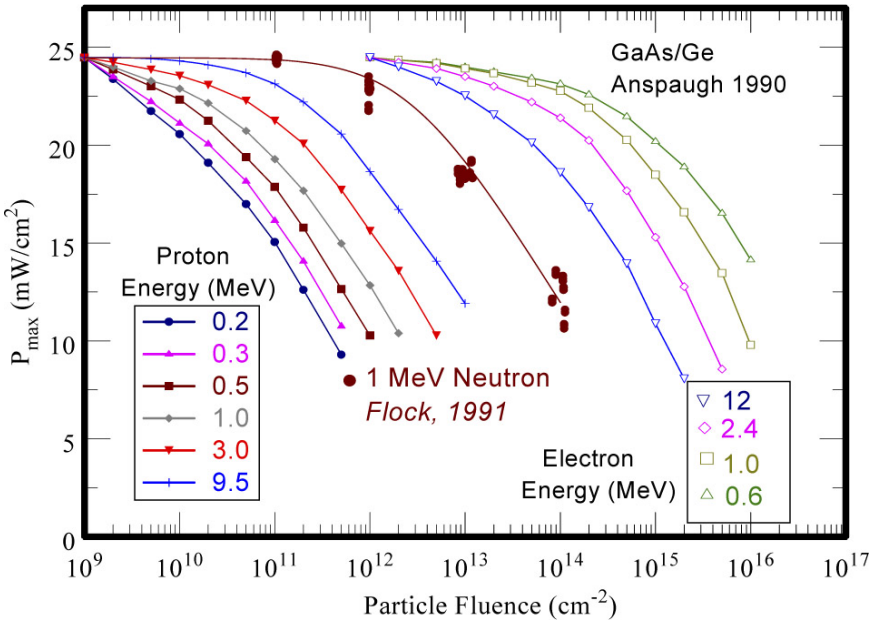

Figure 1.3: Reduction in max power output of solar cell junctions after being bombarded with various levels and types of radiation. Taken from Walters (2011).

to Earth. In the past low orbit satellites have been used to detect electron precipitation, such as SAMPEX (Jones and Rasch [1990]), but this is a very costly solution.

Section 3 introduces the Balloon Array for Relativistic Electron Losses (BARREL), a collaboration between five universities that will launch high-altitude, zero-pressure polyethylene balloons to circle Antarctica during the RBSP mission. As the relativistic electrons enter the atmosphere, they decelerate and produce x-rays which can be detected by the balloon array.[Millan et al., 2011] All of the data collected by the balloons are sent via satellite to the UCSC campus where it is stored on a secure computer. My work with BARREL is to develop and maintain software that will process and disseminate these data in near real time. The main components that make up my software are background services that translate the raw data and look for errors (Sections 3.4.2 and 3.4.3) and web interface for viewing real-time and archived data (Section 3.4.4).

2 Plasmasphere, Magnetosphere, and the Radiation Belts

In order to understand the region of space affected by the magnetosphere, two new coordinate systems must be introduced. First, is a way of specifying space that contains a specific magnetic field line called L-Shell. Figure 2.1 illustrates how the location of the line is measured. Starting at the equator, the distance to a field line is measured in units of Earth radii. That distance defines the L value for the entire field line as it comes in towards the poles. So, when referring to L=2, what is being specified is the region of space containing a field line that passes through the equatorial plane at two Earth radii. ‘

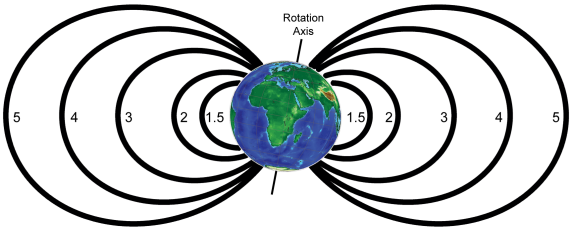

Figure 2.1: Diagram of L-Shell coordinates. This coordinate is defined as the number of Earth radii between the equator and the field line.Taken from Wikipedia under GNU Free Documentation License.

The second coordinate that is important is magnetic local time, or MLT, as shown in Figure 2.2. Looking at the Earth relative to the Sun, the lit side is the dayside and the dark side is referred to as nightside. Dawnside is the area that is moving from nightside to dayside as the Earth rotates and, conversely, duskside is where the Earth rotates from dayside to nightside. These labels,

along with numerical representations of MLT times are shown in Figure 2.2.

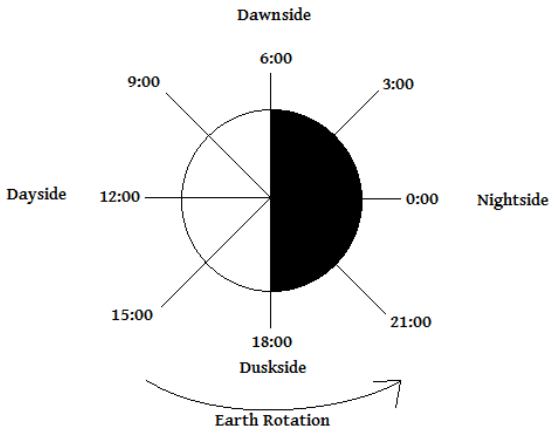

Figure 2.2: Map showing magnetic local time coordinate system.

The structure of magnetic fields and charged particles surrounding the Earth is complex and interdependent. Starting from the Earth and moving outwards we start with the plasmasphere. This region is filled with cold, dense plasma that co-rotates with the Earth. It extends out to approximately L=4 where the density of particles suddenly drops off at what is called the plasmapause. The inner radiation belt is a region of trapped particles inside the plasmasphere extending out to L=2.5. Beyond the inner belt, extending to approximately L=4, there is an empty region called the slot. After the slot is the outer belt which is full of high energy electrons and extends out to L=6. All of these regions are made possible by the Earths magnetosphere which trapps charged particles along its field lines. These lines, however are dynamic due to influences from the Sun. Interactions between the Sun and the Earth's fields result in a number of instabilities and fluctuations within the regions governed by the magnetosphere.

2.1 Geomagnetic Storms

Unlike the Earth, the Sun's magnetic field is quite variable. Field lines reaching from the Sun to our own magnetosphere, called interplanetary magnetic field lines or IMF, can play an

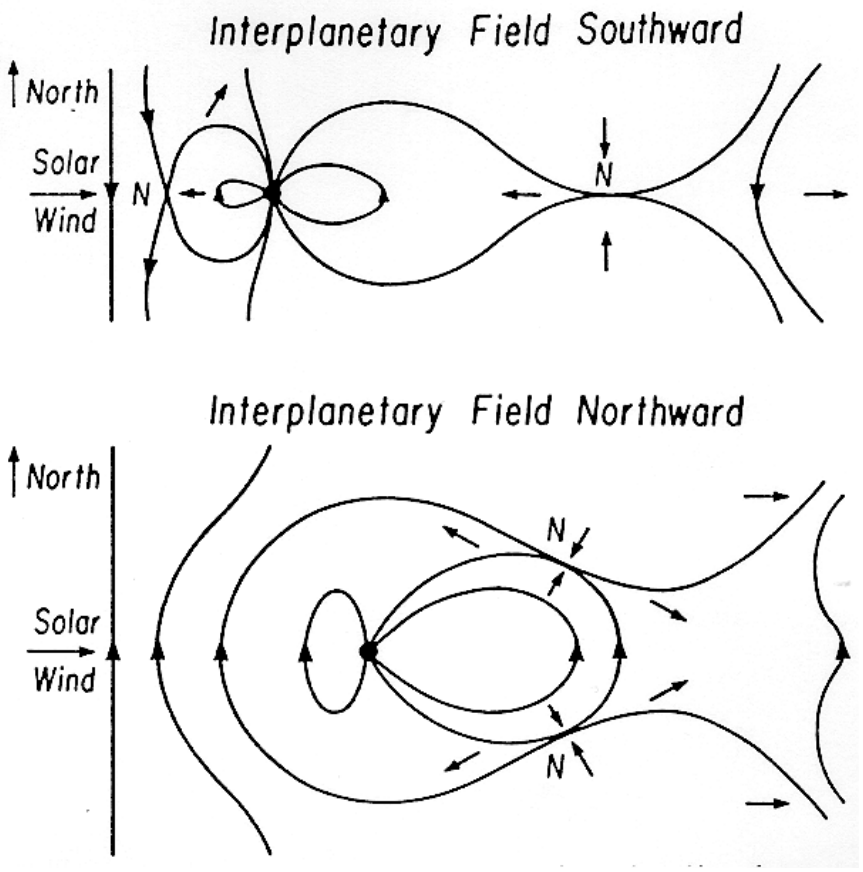

Figure 2.3: Top: Southward IMF opens and connects to the Earths magnetosphere. Bottom: Northward IMF showing compression in the sun facing magnetosphere. Taken from Russel et al. [1995].

important role in the energy density of the magnetosphere. If the IMF is oriented parallel to our own field lines (Northward IMF) the sunward facing side of our magnetosphere is compressed as the field lines push away from each other. However, if the IMF turns antiparallel to our own field (Southward IMF), it will open some of our sunward field lines and connect them to the Sun's field lines. This will allow some of the solar magnetic field to be connected to our own allowing large quantities of plasma to flow into the magnetotail [Smith and Lockwood, 1996]. These are some of the characteristics that form what is referred to as a geomagnetic storm and can be seen diagrammatically in Figure 2.3. Geomagnetic storms can be accompanied by a series of substorms which are largely identified by activities in the magnetotail.

2.2 Substorms

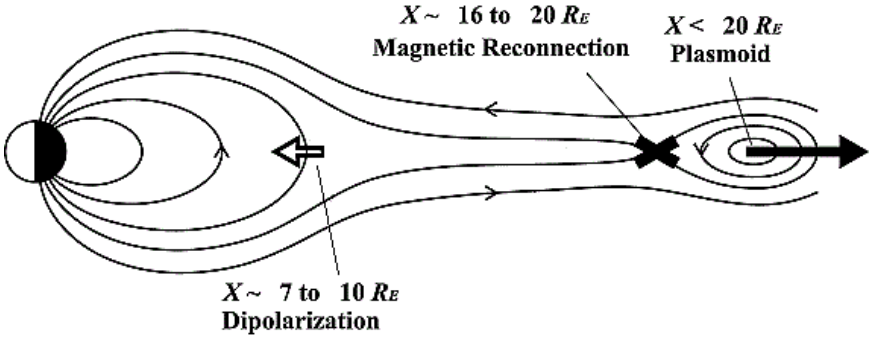

Figure 2.4: Schematic of tail dynamics during a substorm. Adapted from Miyashita et al. [2009]

A substorm can be broken up into three main stages: Growth phase, expansion phase, and the recovery phase. During the growth phase solar wind feeding the magnetosphere will cause the tail to become increasingly elongated. Energy will build up in the tail as it is blown back and stretched out by the solar wind. The expansion phase, also known as the onset of the storm, begins when the tail has been stretched so far that the magnetic field lines reconnect mid way through the tail at about 20 Earth radii. Energy building up in the tail causes an isolated region of plasma, called a plasmoid, to be formed at the end of the tail and ejected. As the plasmoid is ejected, the night side of the magnetosphere will rush towards Earth, reorganizing itself into something closer to the dipole model in Figure 1.1 through a process known as dipolarization. The dipolarization results in a large release of energy that was stored in the magnetotail and can accelerate trapped particles to very high, relativistic, energy levels. The recovery phase consists of the magnetosphere returning to the pre-substorm state after the dipolarization.[Miyashita et al., 2009, Goldstein, 2006] A graphical overview of this process can be seen in Figure 2.4.

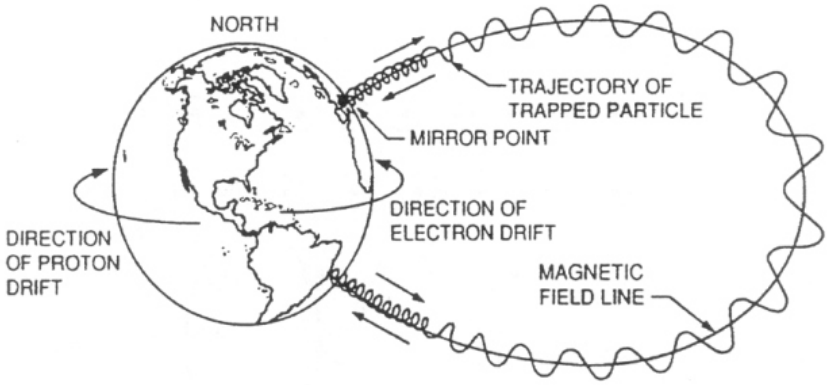

Figure 2.5: Three motions undergone by charged particles trapped in a magnetic field. Taken from Walt [1994]

2.3 Trapped Particles and the Adiabatic Invariants

The inner and outer belts are formed because charged particles interact with the magnetic field lines and can become trapped. While trapped in the field a particle's path is governed by three motions called the adiabatic invariants: drift, bounce, and gyration as shown in Figure 2.5. These are called invariants because, under normal conditions, they are conserved. That is, if a particle is trapped its motion will remain unchanged unless a force acts on the particle on a shorter timescale than that of the invariant.

2.3.1 Gyration

The invariant of most importance to this paper is that of gyration or cyclotron motion. If a charged particle is moving near a magnetic field its motion will be influenced by the Lorentz force

$$\mathbf{F} = q[\mathbf{v}X\mathbf{B}] \tag{2.1}$$

This force causes a particle that has a velocity component perpendicular to a nearby field line to gyrate around that line. If the particle also has a parallel component to the velocity it will follow a helix pattern as it travels along the field from one pole to the other. The gyrofrequency, ω_g, and gyroradius, ω_g, are given by Schindler [2007] as

$$\omega_g = \frac{|q|B}{m} \tag{2.2}$$

$$r_g = \frac{mv_\perp}{|q|B} \tag{2.3}$$

For electrons, the period of this motion is on the order of milliseconds so there are a limited number of forces that will be able to violate the invariant.

2.3.2 Bounce

As a result of gyration and conservation of magnetic moment, polar bounce will occur. Using equations 2.2 and2.3 Schindler [2007] shows that the conserved magnetic moment is give by

$$\mu = \frac{\frac{1}{2}mv_\perp^2}{B} \tag{2.4}$$

As the particle travels closer to one of the poles, the magnetic field lines start to converge. This convergence causes an increase in field strength seen by the particle. The magnetic moment, being a conserved quantity, requires an increase perpendicular velocity for any increase in field strength. As a result of magnetic fields not being able to do work on a charged particle, the increase in $v_\perp$ must be accompanied by a decrease in $v_{||}$. If the cyclotron motion is strong enough, the particle will stop come to a full stop. This decrease in $v_{||}$ can be associated with the Lorentz force. A converging **B** implies a component of the field that is pointing radially inward. The velocity of the particle crossed with the radial component of **B** results in an axial force directed away from the pole. Once the particle has been slowed to a stop the Lorentz force continues to act on it and reflects it back along the field line. The parallel velocity of particle determines the timescale of the bounce motion and tends to be on the order of seconds.

Plotting $v_{||}$ against $v_\perp$ as in Figure 2.6 gives us the loss cone. Any particle whose velocity falls within the loss clone will not experience bounce and will be lost to the atmosphere. Conversely, any particles outside of the loss cone are trapped. The size of the cone represents the maximum pitch

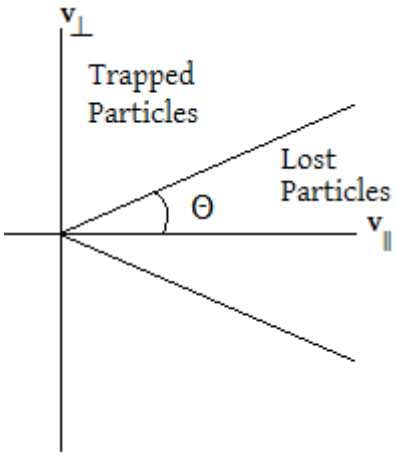

Figure 2.6: Loss cone for charged particles interacting with magnetic field lines formed from the ratio of field strengths.

angle a charged particle can have relative to the field line. This maximum pitch angle is determined by the ratio of the field strength where the particle is observed to the maximum field strength it will experience as

$$\Theta = sin^{-1}\left(\frac{B_{min}}{B_{max}}\right)^{2} \tag{2.5}$$

Violations of these invariants can cause particles to be scattered into loss cone. This will allow previously trapped particles to be lost to the atmosphere. This type of loss, at relativistic energies, is the main focus of the BARREL project and this paper.

2.3.3 Drift

Charged particles trapped in the magnetosphere traverse curved field lines. This curvature leads to two different types of drift that will cause electrons to move eastward and ions to move westward. Moving from the disperse field lines at the equator towards the concentrated field lines at the poles leads to a drift caused by the gradient of **B** given by

$$v_{\bigtriangledown B} = \frac{\epsilon_{\perp}}{qB}\frac{\mathbf{B}X\bigtriangledown\mathbf{B}}{B^2} \tag{2.6}$$

The second kind of drift is the result the field lines having curvature. A particle following a radius of curvature, R_c, will experience a drift of

$$v_R = \frac{2\epsilon_{||}}{qB}\frac{\mathbf{R_C} X \mathbf{B}}{R_C^2 B} \tag{2.7}$$

in order to provide the needed centripetal force so the particle can follow a curved path. In both cases ϵ refers to the kinetic energy of the particle.

Drift is the longest timescale invariant of the three, taking minutes to perform a cycle. This results in negatively charged electrons having an eastward azimuthal motion and positively charged ions drifting westward. Because the timescale drift is so long, ULF waves can break the drift invariant. Invariant violations caused by these waves result in particles being diffused radially. This can both be a source of particles to the radiation belts as well as remove particles from them, although the losses are not caused by scattering into the loss cone and are not of great interest to this paper. [Millan and Thorne, 2007]

2.4 Loss Mechanisms

I will explore three types of loss mechanisms here: plasmaspheric hiss which creates the slot between the inner and outer radiation belts; The whistler chorus responsible for generating microbursts, one type of medium energy (and possibly relativistic) electron losses; and EMIC waves which may be causing DREP, a major candidate for relativistic electron losses. These are the mechanisms that BARREL will be investigating in hopes of better understanding energetic events.

2.4.1 Plasmaspheric Hiss and the Slot

In the cold dense plasmasphere, low-frequency radio waves (0.1 - 200kHz) called hiss dominate the morningside. The origin hiss has been debated for some time, however, Bortnik et al. [2008] has recently shown that a good candidate for their source is another wave from further out called

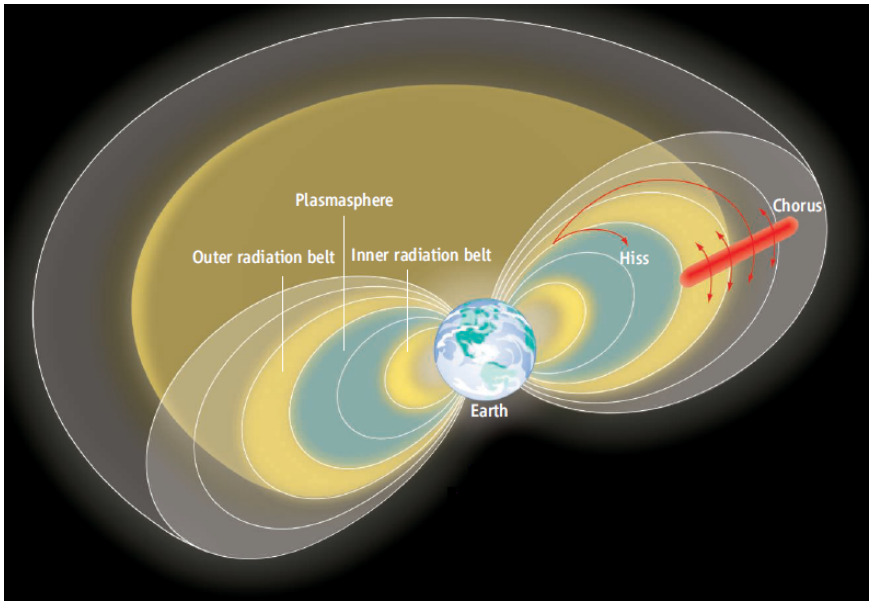

Figure 2.7: A diagram showing the locations of the whistler chorus and hiss with relationship to the plasmasphere and radiation belts. Adapted from Santolk et al. [2009].

the whistler chorus. Using data from the THEMIS satellites, located just inside and outside of the plasmasphere, it appears that there are strong correlations between changes in the chorus and hiss intensities.

The chorus is characterized by coherent whistler waves in the outer radiation belt which a has frequency range of about 100Hz to 5kHz. These waves are also found on the morning side and have a number of sources that are not entirely understood. [Millan and Thorne, 2007] These waves are thought to propagate inwards to the dense plasma where they superimpose on one another forming into the hiss that has been observed.

In the plasmasphere the electron energy that will resonate with hiss is shown by Helliwell [1965] to be dependent on a parameter α^*. This parameter is defined as

$$\alpha^* = 2\frac{B^2}{8\pi N}\frac{1}{m_e c^2} \tag{2.8}$$

This parameter, being proportional to the magnetic field per particle sharply declines upon entering the plasmasphere due to the sharp increase of particle density. The smaller required energy

for electron resonance means an increased number of resonating electrons leading to wave amplification. As the wave propagates inwards it scatters electrons into the loss cone and emptying a region between the inner and outer belts known as the slot. The emptying process has been confirmed by the recent data from the IMAGE satellites as analyzed by Goldstein [2006] where it was seen that the plasmasphere ended where the outer belt began.

A diagram showing the relative locations of how the chorus and hiss fit with the radiation belts and plasmasphere can be seen in Figure 2.7.

2.4.2 Microbursts

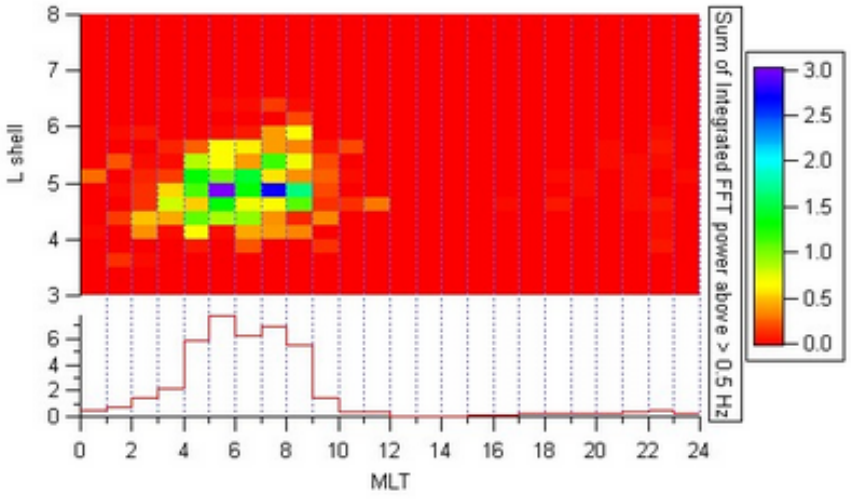

Figure 2.8: SAMPEX data showing distribution of morning microburst events. Taken from Comess [2011].

One important wave-particle interaction that leads to the of scattering electrons from the outer belt are short events called microbursts. These events occur as a burst of several, very short ($< 1s$), electron precipitations around morning MLT where the chorus is predominant as seen in Figure 2.8. Microbursts have long been known as the primary cause of low energy electron precipitation [Rosenberg et al., 1981]. These low energy events are observed to have a strong correlation to fluctuations in the chorus. It has long been established that the whistlers in the chorus are

responsible for scattering electrons into the loss cone precipitating as low energy microbursts.

Until recently, relativistic microbursts have been something of a mystery. According to Millan and Thorne [2007], previous attempts to link high energy microburst to the chorus have failed. However, in the last few years a new type of whistler, the high amplitude whistler, has been discovered. Using data coolected by STEREO-A and STERO-B, Kersten et al. [2011] have shown that these types of waves occur in the dawnside. The SAMPEX satellite was able to observe nearby relativistic microbursts at very nearly the same time showing a similar time signature as seen in Figure 2.9. The duration of the whistler mode waves is on the sub-second timescale and come in large clusters, just as we see in microbursts. Unfortunately, the satellites were not equipped to time the events precisely enough, so it can not be definitively said that this is the mechanism causing microbursts, but it is the most promising candidate for now.

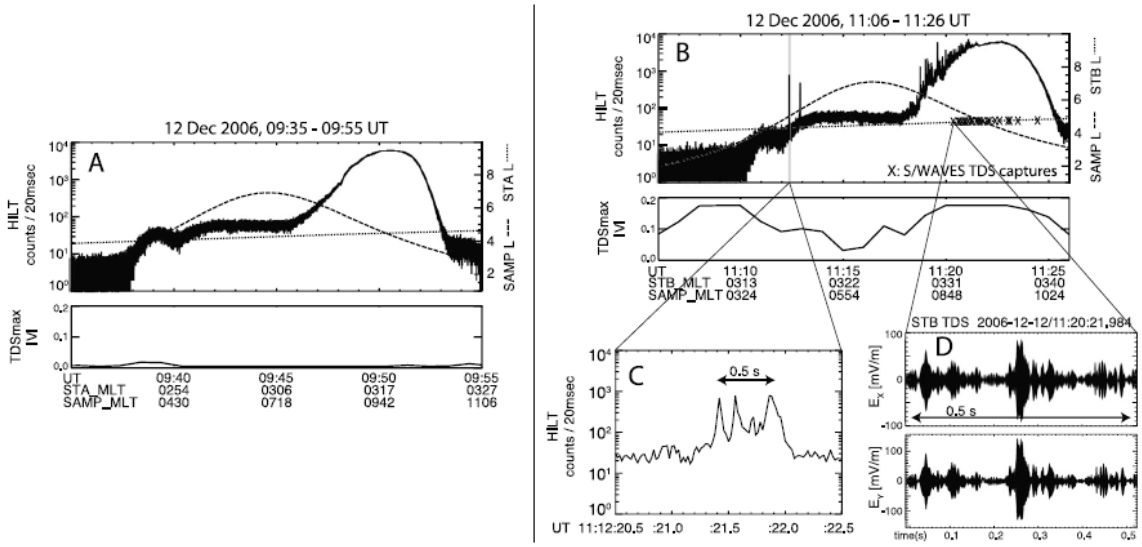

Figure 2.9: Left: SAMPEX data with STEREO data below are showing no microbursts or whistler mode waves. Right: Microburst events in as seen by SAMPEX and the wave capture below. Taken from Kersten et al. [2011].

While it is thought that large amplitude whistlers may be of the same origin as the whistler chorus, there are some distinct differences that must be noted. First, as the name implies, the amplitude is much higher than the chorus. High amplitude waves are observed in excess of 300mV/m as opposed to approximately the 30mV/m amplitude of the chorus. Second, the chorus waves are

always seen propagating parallel to the field lines, whereas the large amplitude waves are oblique moving at 45-60° with respect to the field lines. [Cattell et al., 2008, Kersten et al., 2011] These differences must make us consider the possibility of an origin unique from the chorus waves.

2.4.3 EMIC Waves and DREP

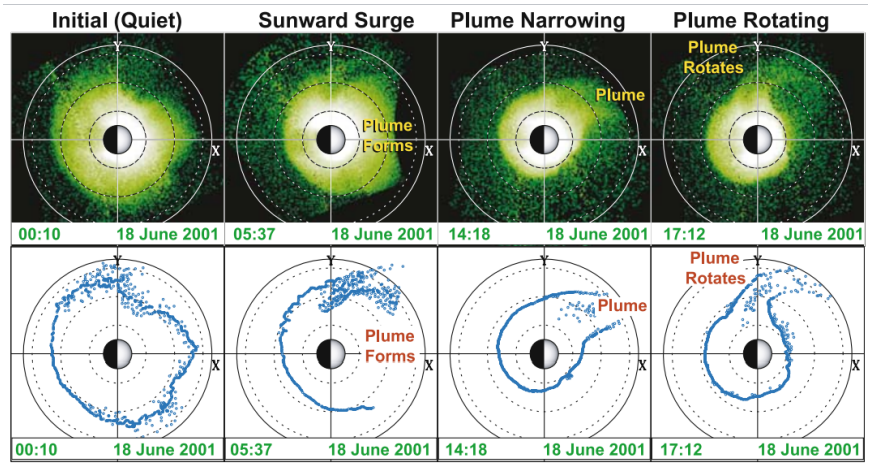

Figure 2.10: Top: Plasmasphere images showing the June 18, 2001 event of a plasma plume forming and being dragged eastward to the duskside. Green dots show plasma densities and the dotted lines indicate approximate L=2 and 4. Bottom: Blue lines bound the outer plasmasphere as manually extracted from images in top row. Adapted from Goldstein [2006].

Electromagnetic ion cyclotron waves, or EMIC waves, are disturbances that readily propagate through the plasmasphere, occurring more often during geomagnetic storms near dusk.[Millan and Thorne, 2007] During a storm, the dayside facing field lines are opened by the southward IMF, thus the containment of the plasmasphere is weakened allowing it to bulge sunward. Furthermore, there is an electric field, oriented from dawn to dusk, seen by the particles that make up the solar wind. This field is a result of the particles experiencing a $\mathbf{v}X\mathbf{B}$ force. However, in their reference frame they are stationary it it appears as an electric field. This externally applied field in conjunction with the Earth's own internal electric field interact with the plasmasphere and drags the bulge out to the dusk side forming a plume as in Figure 2.10. This plume will reach beyond the nominal plasmapause location into the outer belt at L=6. [Goldstein, 2006, Grebowsky, 1970]

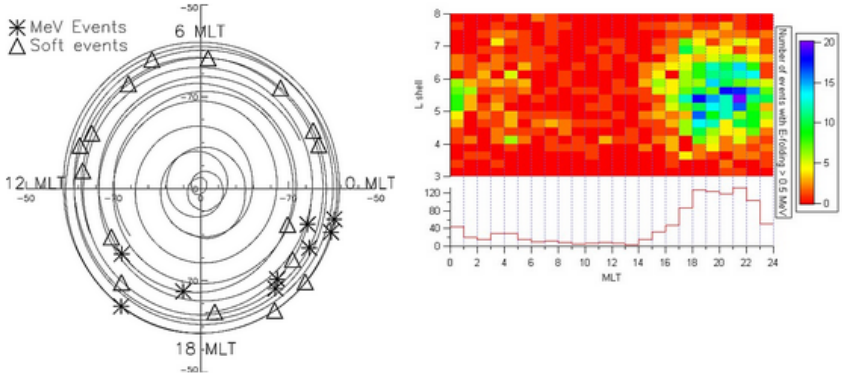

Figure 2.11: Left: Electron precipitation events seen by the MAXIS balloon flight. Triangles are low energy events while asterisks are DREP. It is readily seen that DREP only occurs in the dusk region while soft events can happen anytime. Right: Similarly, these SAMPEX satellite data show DREP events seen from space. Again these events are only seen in the dusk region. Adapted from Millan et al. [2002] and Comess [2011].

If an EMIC wave propagates through the duskside while the plume has extended to the outer belt it has the ability to resonate with relativistic electrons and scatter them into the loss cone. This event, called Duskside Relativistic Electron Precipitation or DREP, is a candidate to be one of the main causes of relativistic electron losses from the outer belt.[Millan and Thorne, 2007] Figure 2.11 shows the spatial distribution of precipitation events as seen by the MAXIS balloon flight. Confirming DREP as a major source of electron losses will be a primary objective of BARREL.

2.5 Microbursts vs. DREP

There are a number of important differences between microburst events and DREP. The first, and most apparent, are the timescales over which they occur. While many microbursts can occur over the course of minutes, each individual event is actually only a fraction of a second long. DREP, on the other hand, is characterized as a single, long event that lasts on the order of minutes. These timescales are compared in Figure 2.12.

The two events also vary greatly in their spectra. As viewed from a balloon during the MAXIS mission, Figure 2.13 shows that DREP has a much harder energy spectrum than microbursts.

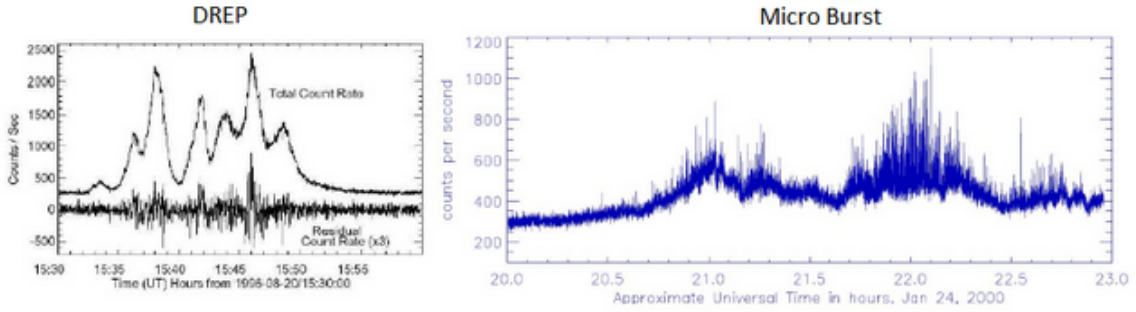

Figure 2.12: Left: DREP timescale and shape showing one long event that lasts minutes. Right: Many microburst events, each lasting less than a second, producing a bursts for many minutes. Adapted from Comess [2011]

It should be noted that from a balloon we do not see relativistic microburst even though satellite data indicate they are somewhat common. It is thought that "relativistic microbursts" that have been seen are simply the ordinary microbursts that contain a small amount of high energy particles. Since the bulk of particles are still low energy, the high energy portion may be lost during detection. This is because balloons can only see electrons via bremsstrahlung which created by high energy particles being deflected as they enter the ionosphere. Deflection results in a loss of kinetic energy and a corresponding photon emission. The photon will then undergo Compton scattering as it moves through the atmosphere to the balloon where it will be detected by the payload. Each of these steps causes energy loss which means a loss of spectral information. That is to say, the detected energy will be less than that of the precipitated particle because the bremsstrahlung will only be as energetic as the amount of kinetic energy that is lost; each Compton scatter transfers energy to the colliding particle; and the detector itself has signal loss. Evidence of this is seen by noting that we never see a microburst event with an e-folding energy of more than 200keV. [Comess, 2011]

Further differences between the two mechanisms can be seen when comparing the levels of precipitation at different energy levels. Comess [2011] uses SAMPEX data to show that the onboard HILT detector records nearly twice as many 1MeV electrons being precipitated by microbursts when compared to DREP. However, at 1.5MeV and above DREP is seen to have over twice as many precipitated electrons than microbursts.

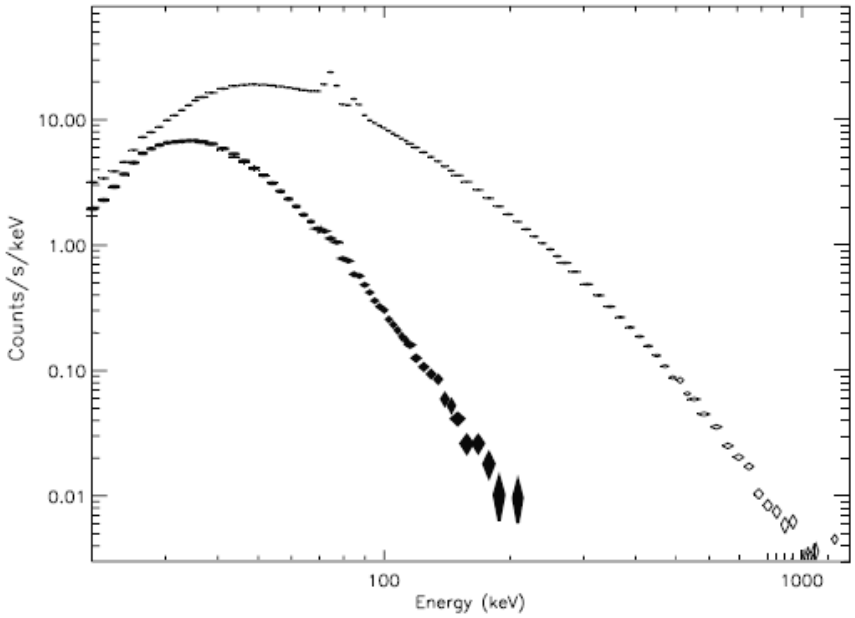

Figure 2.13: Solid Diamonds: Spectrum of a typical microburst event as seen by balloon-borne detectors. Hollow Diamonds: DREP event showing a much harder spectrum. Adapted from Millan et al. [2002].

3 BARREL

Starting in 2012 NASA will launch the Radiation Belt Storm Probe (RBSP) in an attempt to better understand the dynamics of the radiation belt and electron precipitation.This mission will measure many of the conditions in the outer radiation belt as outlined in Ukhorskiy et al. [2010]. One problem is at the altitude NASA will be flying the RBSP mission, the loss cone for precipitated electrons is only 7° wide. This makes it nearly impossible to determine if detected electrons are lost to the atmosphere. There is a need for a low altitude probe that can detect losses, similar to the SAMPEX satellite. A balloon mission to work in conjunction with RBSP, the Balloon Array for RBSP Relativistic Electron Losses (BARREL) was the answer.

3.1 Why Balloons?

The main issue with flying a satellite is cost. The entire BARREL mission is just a fraction of the cost that it would take to send a low orbit satellite up. However, in addition to the cost savings, there are many other important reasons to choose balloons. Balloons tend to stay in the same area allowing a longer look at an event rather than just a quick snapshot from a satellite that flies by. We can also fly an array of balloons in order to get an understanding of spatial dispersions of loss events. Up to 16 payloads will be circling the Antarctic continent at a time, each for at least a week. This array of balloons will provide an excellent mapping of precipitation to magnetic field lines and RBSP. Finally, balloons are beneficial in that they see precipitation via bremsstrahlung so any electrons detected are guaranteed to be in the loss cone.

3.2 Onboard Instruments and Equipment

Each payload will carry three main science instruments, a host of internal sensors, and a power source. Incoming x-rays will be detected by a 3" x 3" sodium iodide scintillator with a range of 20keV - 7MeV which will have an effective area at 1MeV of $16cm^2$. The detectors produce three types of data each trading time and energy resolution. First four energy channels (10-180, 180-550, 550-840, 840-1500 keV) output counts per second every 50ms. Greater energy resolution is gained by accumulating data for 4 seconds into 48 logarithmically spaced channels. Finally, energy is binned into 256 channels over an accumulation of 32 seconds giving. [Millan et al., 2011]

A magnetometer will be on board each payload to help map magnetic field lines, detect substorms, and possibly EMIC waves. The sensor used is a Bartington three-axis device with extremely low noise ($20pT$). The output is analog, so an additional board made at UCSC is employed to quantize and encode these data into a floating point format suitable for transmission. The sensor also includes a temperature sensor to help correct any fluctuations due to device heating. A Lassen-SQ GPS unit is used for balloon location and time stamp of events. Its the payload location in addition to magnetometer readings will be used to help map the current L-shell of the payload. [Millan et al., 2011]

Power is supplied via four solar panels which use a DC-DC converter and charge controller to power the payload and battery bank. The payload should consume $\approx 8W$ of power which has been established during test flights.

Temperature, current, and voltage data are constantly monitored for all critical parts of the payload. These data are multiplexed as mod40 and transmitted once per second so at any given time one of these 'housekeeping' datum will be up to 40 seconds old. These sensors are critical to ensuring the proper operation of the payload.

All of the information is organized into 194-byte (96 words) frames that are transmitted every second. Transmissions occur via an iridium satellite network and are received by the Mission Operations Center (MOC) located at UCSC.

3.3 Monitoring Process

Incoming data needs to be monitored continuously to check for any critical failures in the payload as well as any interesting science events that may occur. This monitoring is done via web applications provided by the Science Operations Center (SOC) and can be accessed from anywhere using the internet. Two Mission Monitors will be watching these data at any given time and one duty scientist will always be on call. Reports will be filled twice per hour by Mission Monitors indicating any anomalous data. If the SOC indicates any critical failures the Mission Monitor is alerted and instructed by the software to contact the duty scientist. If the Mission Monitor fails to acknowledge this alert, the SOC will contact the duty scientist via email and/or text message. Development of the SOC software has been my primary contribution to BARREL.

3.4 Ground Station

The BARREL SOC software package is used to collect, archive, and disseminate the information in the MOCs raw data files. Local and remote users can see a live feed of the newly received information as it is written and use a number of visualization tools to analyze archive files. This is done by providing three main functions: near real-time conversion of incoming binary data files into ASCII archive files; data monitoring and duty scientist notification of values that exceed maximum limits; and a web interface for viewing live and archived data in a number of different ways.

The supporting hardware for this system consists of two SOC computers running Fedora 11 on dual-quadcore servers and 2GB of RAM. They share a network attached storage device (SOC-NAS) which stores all the output files to be used by web applications. Five laptops, up to four payloads per laptop plus one spare, running Windows XP make up the MOC hardware. They also share a network attached storage device (MOC-NAS) and are protected from the outside world through a firewall.

As the MOC receives raw data, it writes binary files to the MOC-NAS. These new data

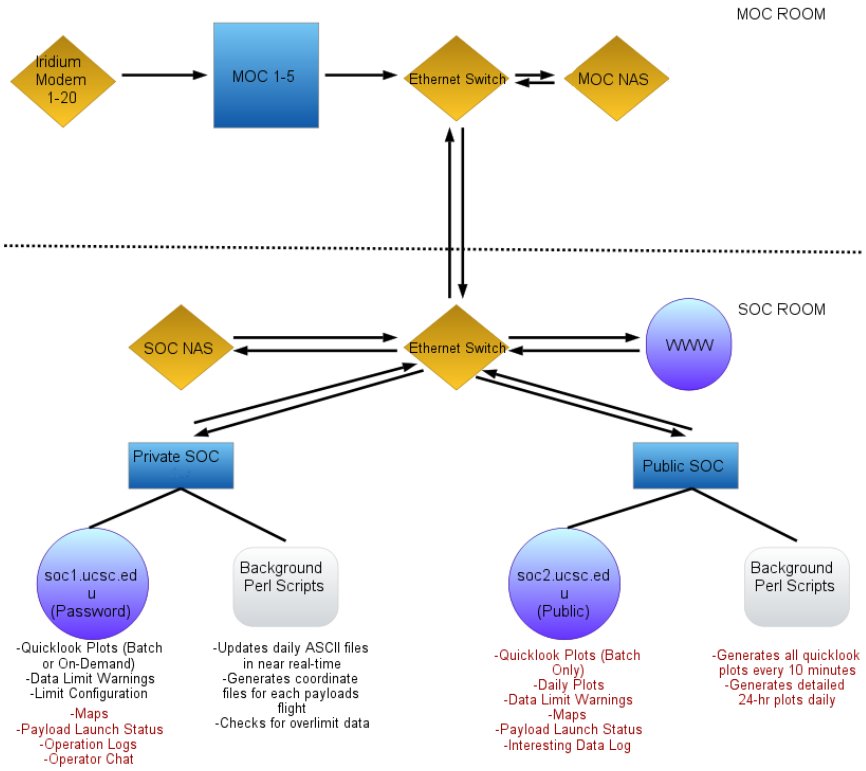

Figure 3.1: Flowchart of how the SOC and MOC components interact with each other.

are detected by the SOC which converts them from binary to ASCII format and saves them to a number of different files on the SOC-NAS. These files are then read by an alert generator that will update a status file indicating any values that are out of range. The alert generator is configured to notify the Mission Monitor if any data are too far out of range. If this this is ignored, a duty scientist will be notified via text message or email. This status file, as well as the various ASCII data files, are used by the web interface to display information about payload health, quick look and archive plots, maps, and a live feed of data values as they are being extracted.

The SOC web-interface software runs in two modes, each of which is set to govern the operations of an entire SOC computer: admin mode, which is always run under password protection, and public mode. Admin mode is used by the duty scientists only for controlling certain functions having to do with how the alert generator works and what payloads are available for monitoring.

Public Mode is read-only with respect to these parameters, and is configured for the use of Mission Monitors and the general public. Figure 3.1 gives a flowchart showing the interdependence of the SOC and MOC components.

3.4.1 Configuration Files

There are two types of configuration files in the SOC: a system configuration file and data limit configuration files. The limit configuration files can be viewed and edited in the Configurator which is part of the web interface. These limits are used by the alert generator and the various data viewing tools and will be discussed in the appropriate sections.

Many of the SOCs functions are controlled by the system configuration file. Since much of the SOC software is written in Perl, this file is set up as a module that resides in one of the shared Perl library directories on the SOC machine. Important values contained in this file are: a list of payload names and reference indices; SOC mode; directory locations; settings for how alerts are generated and binary files extracted; and scaling information for housekeeping data. In addition to holding configuration values, this file also holds common Perl subroutines that can be exported to various programs.

3.4.2 Data Extraction and Storage

When the MOC starts a call to its payload, it creates a new binary file saved both locally and on the MOC-NAS. The files are named with a time stamp and separated into folders based on the date. The length of each file is variable as it will continue to grow as long as the call is connected. As soon as the signal to the payload is lost, the file is closed and a new one started.

The SOC continuously monitors the MOC-NAS for any changes to the file structure. If any new data are detected, it is immediately collected and translated. The translation process happens one frame at a time, each frame being written to the end of two day-long archive files (One for housekeeping, one for science data) as well as file containing the one frame worth of the newest data.

That is, if an incoming frame does not contain a certain value, the previous one is kept with an asterisk appended to indicate the carryover. The day-long archives are used by all plotting programs and the alert generator, while the single frame file is used by the live data feed.

A few modifications are made to these data during extraction in an effort to make ASCII files immediately useful. First, because the GPS data are multiplexed (mod4), the time stamp only comes in once every four seconds. Part of the extraction process is to fill in the missing values by adding one second per frame, since the last time. If the times tamp somehow becomes out of sync, it will correct itself when the next time stamp arrives so no more than four frames should be incorrect. Also, most of the telemetry data needs to be decoded somehow. Because the x-ray spectra comes at a higher time resolution than frames are transmitted, they occupy multiple words per frame which are combined for ease of use with the SOC. Also, these housekeeping data need to be rescaled based on the values found in the SOC's configuration file.

We exploit the SOC's multi-core processors in order to run multiple instances of the extraction program simultaneously. Each payload will have its own instance running. The primary reason for this is to help keep all of the data feeds as close to real-time as possible. Having 16 balloons in a que could result in the oldest data becoming outdated beyond what is acceptable when monitoring the payload's critical systems.

3.4.3 Alert Generation

The alert generator is run as one instance for all active payloads as set by the SOC in admin mode. As it cycles through each payload on the list, the alert generator first checks to make sure that the current payload is not on an ignored payload list stored on the SOC-NAS. If the payload is not on the list, then a number of most recent data frames are pulled from the day-long files and organized into a data structure. Theses data are stepped through from newest to oldest and checked against values set in the configuration and determines if any yellow or red alerts are needed to be displayed to the Mission Monitor.

Yellow Alerts

Yellow limits are values that will alert the Mission Monitor to temperature, voltage or current sensors that have gone out of range. Possibly interesting events such as spikes in x-ray counts will also generate a yellow alert. These notifications should be mentioned in the half hour report, but usually does not require immediate notification of the duty scientist. Once a limit has been exceeded for a particular data type, no more values are checked for that type and the alert generator moves to the next. This continues until the data structure has been exhausted.

Red Alerts

In addition to the yellow alerts, we have red alerts that indicate Low Altitude, High Sink Rate, Payload Timeout, and major power failures. If the values set for these conditions is exceeded, the Mission Monitor will be presented with an alert they must acknowledge. Ignoring the alert will result in the SOC trying to contact the duty scientist via text message and/or email. Red alerts are so important because they are indicators that we might loose control of the payload. One situation that must be avoided is a runaway payload floating into foreign airspace. When faced with this situation the only options availability are to wait and hope the problem corrects itself or, as a last resort, cut down the payload. While a red alert will generally not need a payload to be cut down immediately, the duty scientist must be informed of possibly critical failures.

Ignored Payloads

There are times when we may want to see a payloads incoming data but not be alerted to exceeded limits. This will usually occur when a payload is on the ground being tested or after being cut down. For these situations the payload name can be added to a file on the SOC-NAS. Adding a name prevents the alert generator from reading the indicated payload's incoming data and no unnecessary alerts will be sent.

3.4.4 Web Interface

The web interface provides a convenient way for anyone to easily monitor incoming data from the payload. It displays data as a payload status bar that is always at the top of the screen, a live feed of translated values, quick-look plots of recent data, day-long archive plots, maps of entire flight paths, and maps of payload locations at specific event times. In addition to data displays, the web interface includes a tool for setting the limits used by the alert generator called the Configurator, has a link to the BARREL Wiki, and displays important system messages to users.

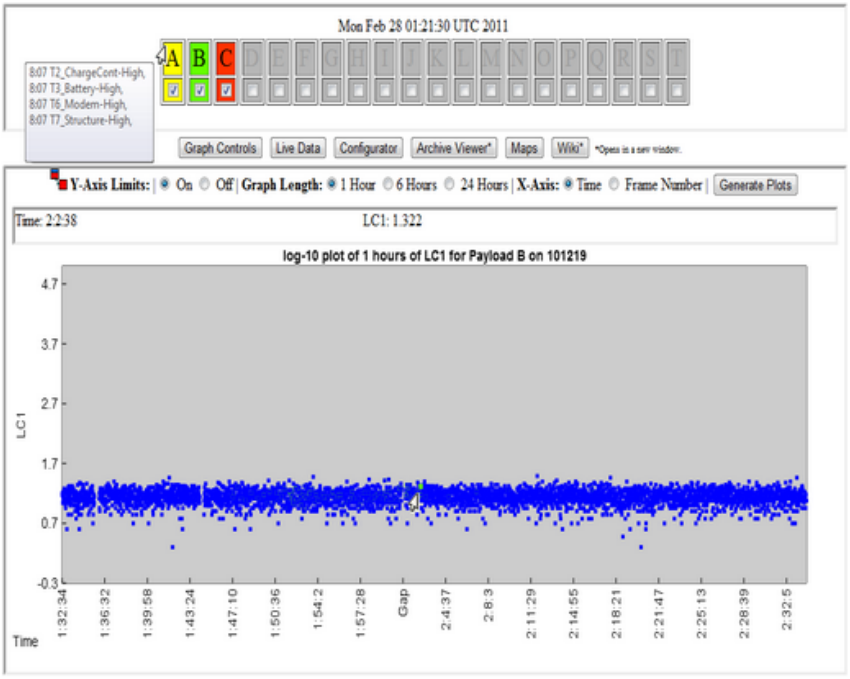

Figure 3.2: SOC in admin mode showing a Status Bar with three payloads activated and quick-look plot. Cursors hovering over a payload box in the Status Bar bring up a description of any alerts, while hovering over a point on the quick-look plot colors it green and displays it coordinate in the box above the plot.

Configurator

In order to set the limits for alert generation and quick-look plot axis limits, there is an online interface called the Configurator (Figure 3.4.4). Opening this interface will display max/min values for voltage, temperature, current, or other science data depending on the particular set of

limits that are to be configured. If the SOC is running in admin mode these values can be changed, otherwise they are read only. The configurator reads the appropriate file from the SOC-NAS and the CSV formatted text is read into a large HTML table with each cell being a text input element prepopulated with the appropriate configuration value.

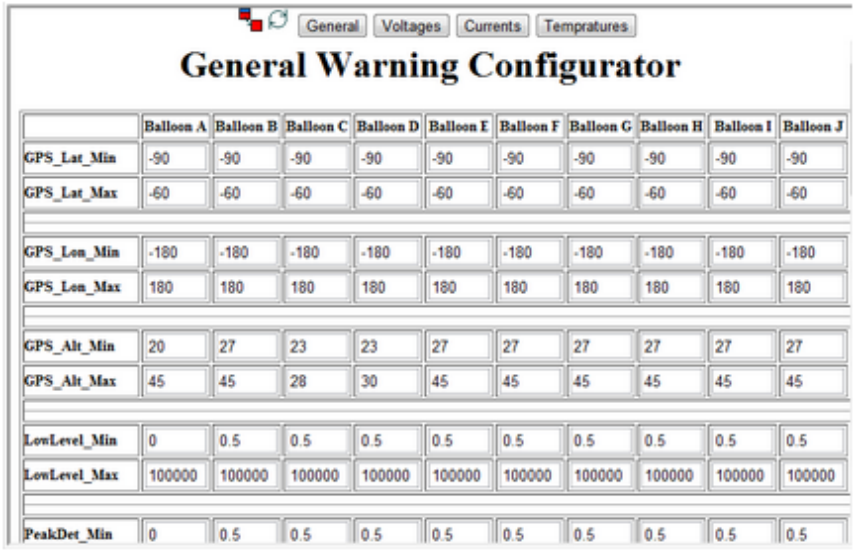

	Balloon A	Balloon B	Balloon C	Balloon D	Balloon E	Balloon F	Balloon G	Balloon H	Balloon I	Balloon J
GPS_Lat_Min	-90	-90	-90	-90	-90	-90	-90	-90	-90	-90
GPS_Lat_Max	-60	-60	-60	-60	-60	-60	-60	-60	-60	-60
GPS_Lon_Min	-180	-180	-180	-180	-180	-180	-180	-180	-180	-180
GPS_Lon_Max	180	180	180	180	180	180	180	180	180	180
GPS_Alt_Min	20	27	23	23	27	27	27	27	27	27
GPS_Alt_Max	45	45	28	30	45	45	45	45	45	45
LowLevel_Min	0	0.5	0.5	0.5	0.5	0.5	0.5	0.5	0.5	0.5
LowLevel_Max	100000	100000	100000	100000	100000	100000	100000	100000	100000	100000
PeakDet_Min	0	0.5	0.5	0.5	0.5	0.5	0.5	0.5	0.5	0.5

Figure 3.3: Limiting values are set for each data type in the Configurator. In SOC admin mode, the tables are editable otherwise they can only be viewed.

Status Bar

The Status Bar, shown at top of Figure 3.4.4, displays color-coded boxes indicating what types of alerts have been generated for that payload. Hovering the mouse over the box will bring up a tool tip that lists the time stamped alerts. This provides the Mission Monitor with a quick way of seeing if any data have gone out of range. A UTC clock is also supplied for the user because that is the timezone all data are recorded in. When the SOC is in admin mode, each payload will also have a check box used to indicate the payload is activate so its data can be viewed and alerts will be generated.

The frame containing the Status Bar will auto refresh every 30 seconds. Each refresh calls a Perl program that reads a list indicating active payloads and what alerts have been generated for

each. Perl will then generate an HTML page to be displayed in the top frame of the SOC display. If a check box is clicked to activate or deactivate a payload, the same Perl program is called with an argument indicating it should edit the active payload list before generating the Status Bar.

Live Data Viewer

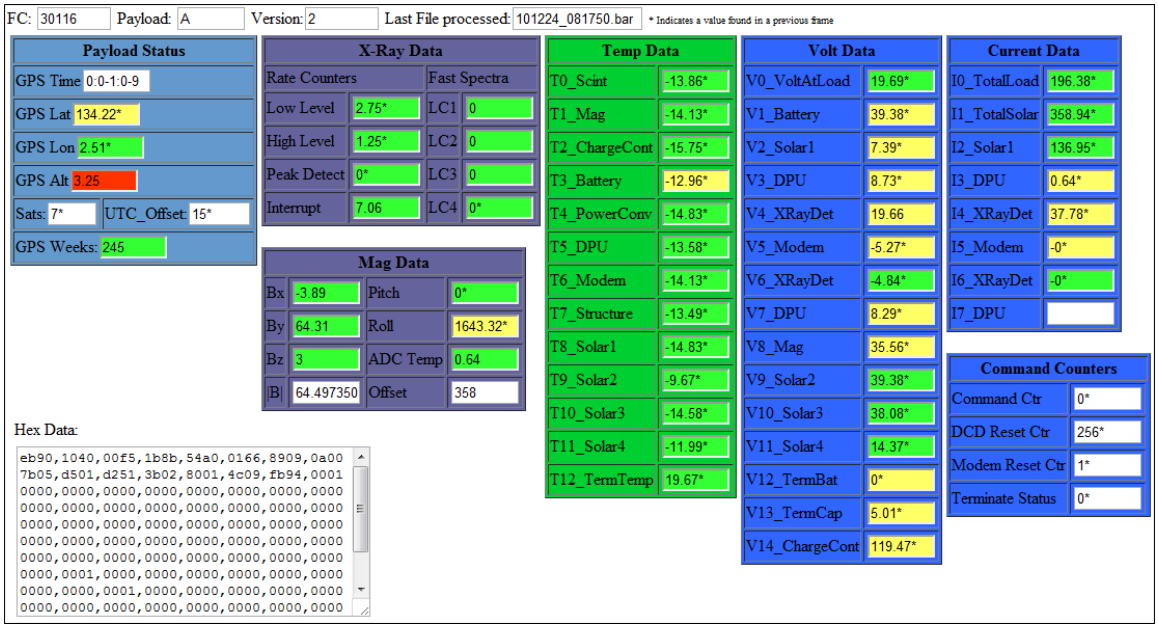

Figure 3.4: Live Data Viewer giving a real-time view of payload sensors and instruments.

One of the easiest way of monitoring incoming data is through use of the Live Data Viewer which can be accesses by clicking on the Live Data button. When activated, a Perl program will accept input in the form of a payload name. If none was sent, it starts with the first payload indicated in the active payload list. Once the payload has been determined, the limits are gathered from the Configurator files and a JavaScript page is generated. The JavaScript will download the newest frame file every four seconds. Each value of this frame is split up and each value checked against the Configurator limits and is displayed in color coded boxes as in Figure 3.4.4. This is organized to appear similar to the MOC terminal which many of the senior members of the team are familiar with. If any value exceeds its limit, the text field will turn yellow, with the exception of altitude

which will trigger a red field. The entire hex formated frame is also displayed in the bottom left of the screen. It should be noted that the hex data may not correspond to all of the translated values. This is because the newest frame file is only updated with the values transmitted in a frame. For example, because GPS data are mod4, at any time only one of GPS_LAT, GPS_LON, GPS_ALT, or GPS_TIME will be current. Anything that is not current will have its previous value retained, but have an * appended to it as an indication that it comes from a prior frame.

By default, the viewer is in Play mode, which means it will update every four seconds. However, a particular data frame can be frozen by clicking the Play/Pause button which will put the viewer into Pause mode. Clicking the button again will start showing the most recent frames again. Next to the Play/Pause button there is a series of radio buttons that indicate which payload is being viewed. Note: Changing limits in the Configurator will not immediately change them in the Live Data Viewer. Because the limits are gathered only once and written into the JavaScript page, the payload must be reloaded for the new limits to take effect.

Graphing

The SOC provides quick-look data plots and maps. Both of these are generated using a custom JavaScript graphing library, which relies on the HTML5 Canvas tag. Because of this requirement, Internet Explorer (as of version 8) is not supported. Recent versions of Google Chrome, FireFox, Opera, and Safari have all been tested and shown to work well.

Quick-Look Plots

The most recent data can be viewed in a quick-look plot with a length of 1, 6, or 24 hours. Clicking on the Quick-Look button, a Perl program is called and generates a JavaScript page containing one chart by default. Drop-down menus are used to select payload, data type, plot length, x-axis label, and whether or not to use the Configurator limits as graph limits. Additional plots can also be stacked each with their own set controls.

When generating a plot, the information set in the controls is used to pull the correct columns of data from the day-long archives for the most recent 1, 6, or 24 hours. This is done with a PHP program which is called via XMLHttpRequest JavaScript API. In order to keep plots from looking compressed, due to dropped calls and data gaps, the plotting program scans the returned data for gaps by looking for sequential frame numbers. Missing frames are replaced with lines with GAP as the frame number and GPS time with all data fields are left blank. Once the data are in the proper format they are sent to the JavaScript library to have the Canvas element filled.

In order to identify exact data point values, plots are generated with a JavaScript event listener that monitors the mouse position relative to the canvas. The mouses X coordinate is converted into an array index for the displayed data. The data point that is located at the array index is highlighted on the plot and has its value shown in a box above the canvas.

Maps

Balloon flight trajectory maps are generated by a Perl program which, when called with no arguments, generates map controls and an HTML5 Canvas element with a blank map of Antarctica overlaid with latitude and longitude grid lines; this is a static image previously generated in IDL. The map controls include starting date and ending date of the flight, payload and color. The default is one payload, but any number of payloads can be added by clicking the Add Payload button. When all of the controls are set, clicking Draw Map reloads the page but uses the control settings as input arguments. The appropriate GPS data are collected from the archive files as matched latitude/longitude pairs by checking frame numbers. Plotting every data point would be excessive, so the GPS time is used to skip 30 minutes of flight time between collected data points. Once the data are collected for each payload, a JavaScript page is generated containing an object that is sent to the plotting library.

Other Tools

The SOC provides links to other useful tools including a wiki and an archive file viewer. The wiki is used to collect mission monitor reports and balloon/flight status reports. The wiki is hosted by a 3rd party and can be accessed by invitation or requesting an account. The archive viewer is a set of tools for working with ASCII CSV files such as the daily archive files. While the tool is hosted on the SOC for convenience, it is not part of the SOC software package and is not necessarily intended for use during the flights, although it sometimes will be.

3.5 Results from Test Campaigns

During the winters of 2009 and 2010 BARREL test flights took place out of McMurdo, Antarctica providing an opportunity to test and improve the SOC software. The 2009 flight saw three major failures, one in the SOC, one in the MOC, and one in the field. The failure in the field was due to a design error in the solar panel. Large thermal gradients seen by the payload each time the balloon would rotate caused flexing because of a miss match in the thermal coefficients of the cell and backing material. The panels would crack and eventually fail. The SOC software was successful in detecting these failures and payloads were cut down when needed.

Unfortunately, ground station also experienced failures in 2009. The SOC, at the time, generated the real-time charts server side, which was a fairly resource intensive process. It was found that during peak usage times enough requests for plots were received by the server that it would hang. Also, at that time, the MOC had SOC's hard drive mounted directly which caused the MOC to hang if the SOC was unresponsive. These two design flaws caused a major failure that lead to the design improvements of offloading image generation to the client and putting an intermediary drive between the SOC and MOC.

In 2010, the test flight was largely successful. There was a critical failure with one payload, but the SOC easily detected it and the payload was able to be cut down before we lost control of it.

One of the batteries became very hot due to an apparent failure in the charge controller, but it was later determined it was a component failure, not a design flaw.

Bibliography

J. Bortnik, R. M. Thorne, and N. P. Meredith. The unexpected origin of plasmaspheric hiss from discrete chorus emissions. *Nature*, 452(6), 2008.

C. Cattell et al. Discovery of very large amplitude whistler-mode waves in earths radiation belts. *JOURNAL OF GEOPHYSICAL RESEARCH*, 35, 2008.

Max Comess. *RELATIVISTIC ELECTRON LOSSES FROM THE OUTER VAN ALLEN BELTS*. PhD thesis, University of California at Santa Cruz, 2011.

F. Darrouzet et al. Plasmaspheric density structures and dynamics: Properties observed by the cluster and image missions. *Space Science Reviews*, 145, 2009.

J. Goldstein. Plasmasphere response: Tutorial and review of recent imaging reesults. *Space Science Reviews*, 124, 2006.

J. M. Grebowsky. Model study of plasmapause motion. *Journal of Geophysical Research*, 75(22), 1970.

R.A. Helliwell. *Whistlers and Related Ionospheric Phenomena*. 1965.

W. V. Jones and N. O. Rasch. Nasa's small explorer program. *Acta Astronautica*, 22, 1990.

K. Kersten et al. Observation of relativistic electron microbursts in conjunction with intense radiation belt whistler-mode waves. *Geophysical Research Letters*, 38, 2011.

R. M. Millan and R. M. Thorne. Review of radiation belt relativistic electron losses. *Journal of Atmospheric and Solar-Terrestrial Physics*, 69, 2007.

R. M. Millan et al. X-ray observations of mev electron precipitation with a balloon-borne germanium spectrometer. *Geophysical Research Letters*, 29(24), 2002.

R. M. Millan et al. Understanding relativistic electron losses with BARREL. *Journal of Atmospheric and Solar-Terrestrial Physics*, 2011.

Y. Miyashita et al. A state-of-the-art picture of substorm-associated evolution of the near-earth magnetotail obtained from superposed epoch analysis. *J. Geophys. Res.*, 2009.

T.J. Rosenberg et al. Conjucacy of electron microbursts and vlf chorus. *Journal of Geophysical Research*, 86, 1981.

O. Santolk et al. The origin of plasmaspheric hiss. *Science*, 324, 2009.

K Schindler. *Physics of Splace Plasma Activity.* 2007.

M. F. Smith and M. Lockwood. Earth's magnetospheric cusps. *Reviews of Geophysics*, 34(2): 233–260, 1996. doi: 10.1029/96RG00893.

D. Summers and R. M. Thorne. Relativistic electron pitch-angle scattering by electromagnetic ion cyclotron waves during geomagnetic storms. *JOURNAL OF GEOPHYSICAL RESEARCH*, 108, 2003.

A. Y. Ukhorskiy et al. Radiation belt storm probes: Resolving fundamental physics with practical consequences. *Journal of Atmospheric and Solar-Terrestrial Physics*, 2010.

James A. Van Allen. The geomagnetically trapped corpuscular radiation. *Journal of Geophysical Research*, 64(11):1683–1689, 1959. doi: 10.1029/JZ064i011p01683.

Martin Walt. *Introduction to geomagnetically trapped radiation*, volume 10 of *Camb. Atmos. Space Sci. Ser., Vol. 10,*. 1994.

R. Walters et al. Modeling radiation degradation in solar cells extends satellite lifetime. *SPIE Newsroom*, 2011.